Advanced Composites and Hybrid Materials (2020) 3:127–140
https://doi.org/10.1007/s42114-020-00140-w

ORIGINAL RESEARCH

Graphene-supported TiO_2: study of promotion of charge carrier in photocatalytic water splitting and methylene blue dye degradation

Neha Singh [1] · Soumita Jana [2] · Gajendra Prasad Singh [2] · R. K. Dey [1]

Received: 13 August 2019 / Revised: 17 January 2020 / Accepted: 20 January 2020 / Published online: 24 January 2020

Abstract
Hydrogen from water provides safe and alternative route for sustainable energy production. The present investigation reports the photocatalytic water splitting using rGO–TiO_2 which efficiently promotes the conversion of solar energy to chemical energy through charge promotion activity. The catalyst was prepared by hydrothermal decomposition process and further characterized for its structural morphology, crystal structure, and photocatalytic properties. Incorporation of GO in the hybrid material found to shrink the band gap of the samples from 3.12 to 2.99 eV. Further, promotion of charge separation is confirmed from the quenching of the emission spectra of the material. The hybrid material with proportionate increment in GO content enhances the H_2 production up to five times higher than pristine TiO_2 material. The catalytic material with 1 wt% GO loading shows decay of methylene blue (MB) dye in aqueous solution at 0.07622 mmol/min. The hybrid material (rGO–TiO_2) found to inhibit recombination center of electron-hole pairs successfully, thus facilitating overall photocatalytic properties of the material for diversified applications.

Keywords Graphene · TiO_2 · Hydrogen · Methylene blue · Photocatalyst

1 Introduction

Designing a new type of photocatalytic material often require successful inhibition of electron-hole pairs' recombination process [1]. Generally, in a single-component photocatalytic material, the quick recombination of the photo-generated charge carriers significantly reduces the conversion efficiency of solar energy into hydrogen energy [2–4]. Increase in conversion efficiency of such kind of catalyst often requires prolongation of lifetime of charge carrier as well as enhancement of charge transfer rate. In this aspect, combination of two dissimilar materials (composite) involving doping/deposition of transition metal, noble metals, or mixing of other semiconductors or supported by any other conducting material such as carbon nanotubes, graphene, and other conducting polymers are immensely useful for fabrication of new photocatalytic materials with improved properties [5–11]. Such kind of structure is commonly known as heterostructure configuration. Heterostructured photocatalytic materials could satisfy both kinetic and thermodynamic stability in addition to providing favorable energy levels for enhancement of redox ability towards charge transfer processes. Absorption of light by heterostructured materials could provide suitable band gap required for improvement of process efficiency.

Graphene–metal oxide composite material possesses good photocatalytic activities in comparison with unadulterated metal oxide. It is mainly due to the unique chemical and physical properties of the material [12, 13]. Combination of graphene oxide with semiconductor photocatalysts such as g-C_3N_4/graphene [14], CdS/graphene [15], and ZnO/graphene [16] could enhance photocatalytic performance by transferring photo-excited electrons from semiconductor surface to graphene oxide sheet, thus delaying the recombination

Electronic supplementary material The online version of this article (https://doi.org/10.1007/s42114-020-00140-w) contains supplementary material, which is available to authorized users.

✉ Gajendra Prasad Singh
gpsinghcuj@gmail.com; gajendra.singh@cuj.ac.in

✉ R. K. Dey
rkdey@rediffmail.com; ratan.dey@cuj.ac.in

[1] Department of Chemistry, Central University of Jharkhand, 835 205, Ranchi, Jharkhand, India

[2] Department of Nanoscience and Technology, Central University of Jharkhand, 835 205, Ranchi, Jharkhand, India

process and augmenting the oxidative reactivity. Titanium dioxide (TiO_2), a proven *n*-type semiconductor, can be considered as an ideal photocatalytic material primarily due to its stability towards various photochemical reactions. Apart from this, material cost, relatively non-toxic nature of the material, and its photocorrosion properties also attributed to the use of TiO_2 in various photocatalytic applications [17–20]. TiO_2 possesses wide band gap (> 3.2 eV), therefore, quick recombination rate of photo-generated charge carrier pairs inhibits its effectiveness towards UV radiation [21, 22]. So, semiconductor materials with wide band gap, noble metals, or sacrificial inorganic electron donors reported to increase the photocatalytic productivity of TiO_2 when used in appropriate amount and condition [22–27].

In this context, the present investigation reports the production of hydrogen from water using reduced graphene oxide (rGO) with TiO_2 as nanocomposites. The material was also used for the study of methylene blue (MB) dye degradation in an aqueous medium. All prepared materials were characterized. The charge promotion activities of the prepared materials were studied using optical spectra. In addition, the kinetics of the MB dye degradation was also studied from rate constant data and half lifetime of the degradation process.

2 Experimental

2.1 Materials

The materials procured for the experiments are listed as follows: graphite powder (325 mesh, fine powder extra pure, Alfa Aesar), hydrochloric acid (HCl, 37%, Fisher), sulfuric acid (H_2SO_4, Fisher 98% v/v, AR grade chemical), potassium permanganate ($KMnO_4$, Fisher), hydrogen peroxide (H_2O_2, 30% v/v, AR grade chemical), and tetra-isopropoxide (TTIP, Merck). All materials were used as received. Deionized water was obtained from Millipore water system. The solvent ethyl alcohol (EtOH, 95%) was procured from Merck and used as such.

2.2 Graphene oxide synthesis

Graphene oxide sheets (GOs) was prepared using commercially available graphite powder following Hummer's method with some modifications [28]. In a typical procedure, 18 mL of concentrated H_2SO_4 was taken in a 100 mL beaker. Subsequently, sodium nitrate (2.0 g) with graphite (0.5 g) powder was mixed to the H_2SO_4 solution, and the entire mixture was stimulated vigorously at 0 °C for 1 h in an ice bath. Powdered potassium permanganate (3.0 g) was added slowly to the above mixed solution, and the entire mixture was stirred continuously for 3 h. The mixture found to form a dark brown color paste. In a subsequent step, 110 mL of deionized water (conductivity, 18.4 MΩ cm) and H_2O_2 (~ 30%, 10 mL) were added to the said mixture following stepwise addition process. The entire solution mixture turned to yellow color dispersion which was washed over and over again with dilute hydrochloric acid and water to eliminate any insoluble salt. Thus, following filtration, a dark brown color solid residue was obtained which was vacuum dried at 60 °C for 48 h.

2.3 Synthesis of TiO_2 nanoparticles

TiO_2 nanoparticles were prepared using environment friendly sol–gel process. Here, TTIP, ethyl alcohol, and HCl were chosen as starting materials. Ethanol (20 mL), in a beaker, was added with 0.5 mL HCl (37% v/v) in a drop-wise manner. The entire mixture was stirred for 10 min. Subsequently, 2.5 mL TTIP was mixed slowly to the above mixture solution. The whole solution mixture was stirred for 4 h to get a transparent gel of TiO_2. The TiO_2 gel was dried in a hot air oven at 100 °C for 12 h. The solid TiO_2, so obtained, was mechanically grinded and calcined at 450 °C in muffle furnace for 1 h. The material was collected and stored in sealed bottle (flushed with nitrogen).

2.4 Synthesis of rGO–TiO_2 binary heterostructured photocatalysts

The reduced graphene oxide (rGO)–TiO_2, a binary heterostructured photocatalyst, was prepared using hydrothermal process. GOs was suspended in mixed water-ethanol (2:1) for 24 h to facilitate exfoliation of material. Further, the re-exfoliation of the exfoliated GOs were done in a mixture of water and ethanol (2:1) solution by ultra-sonication for 2 h. Aqueous solution of re-exfoliated GOs mixed with TiO_2 powder (1 g) was agitated slowly for 2 h to ensure a homogeneous dispersion of the materials. In a subsequent step, 60 mL of homogeneously dispersed solution of GOs mixed with TiO_2 powder was transferred to a Teflon-sealed (100 mL) autoclave for hydrothermal reaction process. The hydrothermal reaction was carried out for 5 h at 180 °C. The hydrothermal treatment process ensures formation of rGO–TiO_2 where TiO_2 could preferably got anchored to the available active sites of rGO. The material was recuperated by sluicing the material numerous times with deionized water and subsequently washed using with ethanol. The material, named as reduced graphene oxide–TiO_2 (rGO–TiO_2), was dried at 40 °C in an oven for almost 2 h. In the process, TiO_2 with selective wt% of graphene oxide (GO) (e.g., 0.5, 1.0, 2.0, and 4.0 wt%) were prepared for further studies. Scheme 1 shows the schematic preparation procedure of rGO–TiO_2 nanocomposite.

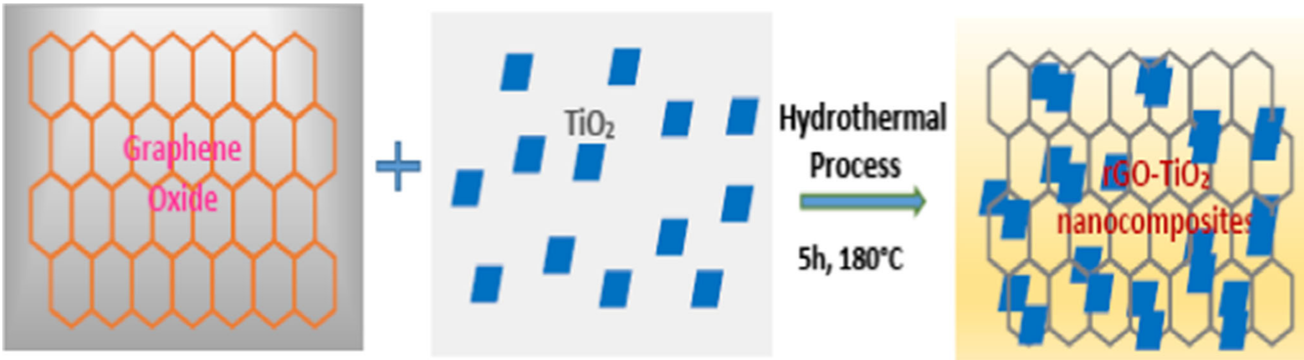

Scheme 1 Schematic representation of synthesis of rGO-TiO_2 nanocomposite

3 Characterization

Characterization of materials were done using various advanced instrumentation techniques. X-ray diffraction (XRD) powder patterns of the materials were recorded using Bruker D8 Advance diffractometer with CuK_α radiation of 1.5418 Å. Shape and size of the sample materials were recorded using transmission electron microscopy (TEM), operating at 100 kV accelerating voltage (Philips). Photo-energy absorption behavior were studied using Carry 500 Diffuse reflectance UV-visible spectrophotometer in the range of 200–800 nm. Raman spectrophotometer, model iHR550, made of Horiba Jobin Yvo, equipped with He–Ne laser as an excitation source, having 632.8 nm wavelength were used to obtain the Raman spectra of the materials. The hydrogenation reaction process was performed in quartz reactor having a well-shaped double wall. A high pressure Hg lamp of 450 W was placed at the center of the reactor as a photon source for the irradiation. In this experiment, fine rGO–TiO_2 (200 mg) powder photocatalyst was dispersed in a 350 mL of aqueous methanol (10% (v/v)) solution containing as scavenger, and the reactor was purged with argon for 30 min to maintain an anaerobic environment inside the reactor. The sample was irradiated by a photon source, and the temperature of the reactor was maintained in an ambient condition by flowing the chilled water at the outer periphery of the reactor. The photocatalysis process was continued for 5 h. Further, in every 1 h interval, the reaction mixture was intermittently analyzed by gas chromatography (GC), model GOW-MAC 580, equipped with All Tech molecular sieve (80/100), 5 A column, and thermal conductivity detector (TCD).

4 Results and discussions

4.1 Structural analysis

Oxidation of graphite results in formation of GO consisting of oxygen functionalities such as epoxy groups, hydroxyl groups, and carboxylic acid groups. These functional groups favor the attachment of metal ions through electrostatic attraction. Here, the successive addition of Ti^{4+} ions to the GO sheets facilitate the growth of titanium in the composite material under hydrothermal conditions. Digital images of the pristine TiO_2 and the reduced GO–TiO_2 are furnished in Fig. 1.

XRD is one of the tool using which phase purity of the derived samples can be investigated. The XRD pattern of the materials is also shown in Fig. 2. Figure 2(a) shows a peak at diffraction angle (2θ) of 15.97°, which corresponds to the reflection plane (002) of GO with calculated interlayer distance of 0.55036 nm. It may be noted that the interlayer distance of graphite was reported to be 0.335 nm. Therefore, the increase in interlayer distance in case of sample material could be resulted due to the presence of oxygen-containing functional groups in addition to intercalated water molecules present in the moiety [29].

Hydrothermally synthesized pristine TiO_2 sample pattern, in Fig. 2(b), indicates the presence of two phases, i.e., anatase and rutile structural phases in the sample material. The diffraction peaks of TiO_2 anatase phase observed at 2θ values (degree) of 25.87, 36.29, 38.49, 48.29, 55.64, 63.14, 69.39, 70.6, and 82.59 are indexed to the reflection from (101), (103), (004), (200), (2 11), (211), (204), (114), and (215) planes, respectively; whereas, the rutile phase peaks observed at 2θ values (degree) of 27.63, 41.41, 54.72, 75.13 are indexed as (110), (111), (211), and (301) planes of reflections, respectively.

All these peaks are found to be fairly consistent with JCPDS no. 21-1276 for rutile and 21-1272 for anatase structure, respectively. Using Scherer's equation (Eq. 1), the average crystallite size (D) of the TiO_2 powder was found to be approximately 25 nm [30, 31].

$$D = \frac{0.9 \times \lambda}{\Delta\beta_{1/2} Cos\theta} \quad (1)$$

In Eq. (1), λ represents the wavelength (Cu K_α radiation = 1.5418 Å), θ is the diffraction angle, and β is the full width at

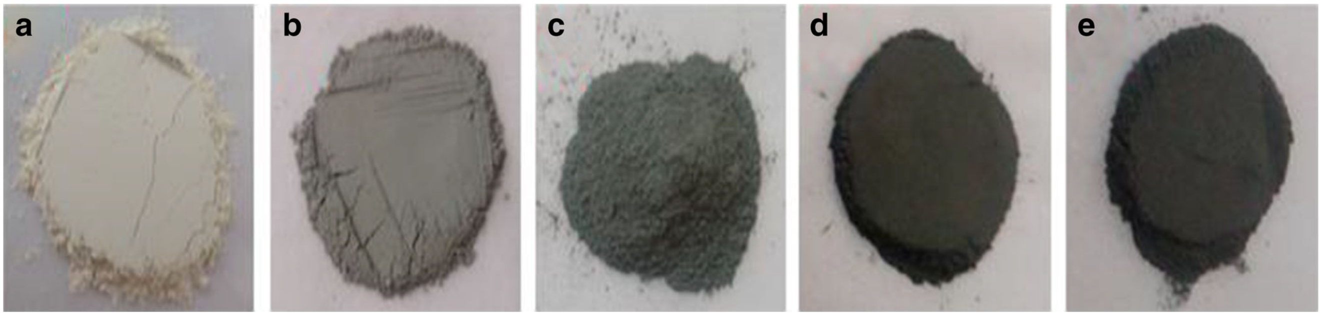

Fig. 1 Digital images of **a** pristine TiO_2; TiO_2 with GO. **b** 0.5 wt%. **c** 1.0 wt%. **d** 2.0 wt%. **e** 4.0 wt%

half maxima (FWHM). It may be noted that no peak of GO is detected in case of rGO–TiO_2 nanocomposite; Fig. 2(c)–(f) indicate the reduction of GO to rGO. However, less quantity of GO, i.e., below the detection limits of the X-ray, or overlapping of the peaks with TiO_2, could also be attributed to the absence of GO peaks in the diffractogram [32].

4.2 Microstructural analysis

The morphology of prepared materials were examined using both field emission scanning electron microscope (FESEM)

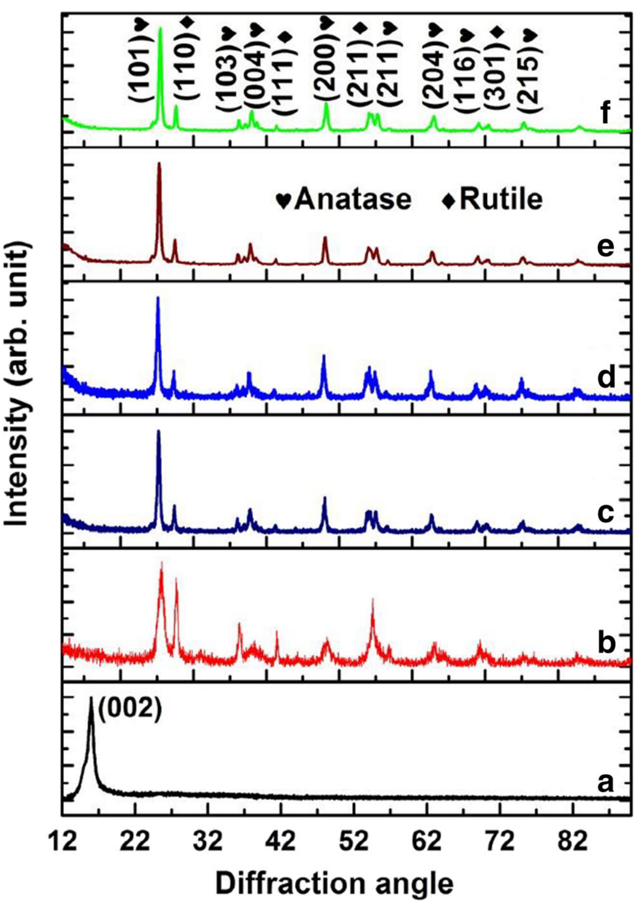

Fig. 2 XRD patterns of (a) graphene oxide (GO) (b) pristine TiO_2, rGO–TiO_2 composite with GO wt%. (c) 0.5. (d) 1.0. (e) 2.0. (f) 4.0

and TEM. The FESEM images of the GO and its composites are shown in Fig. 3a–d. In this aspect, Fig. 3 a and b show SEM image of GO sheet and TiO_2 nanoparticles, respectively. TiO_2 nanoparticles are found to be small in size and largely agglomerated in characteristics. Figure 3 c and d show the loading of the TiO_2 nanoparticles onto the GO sheets. Agglomeration of the TiO_2 particles upon the surface of rGO sheets is also observed in micrograph.

TEM measurement, on the other hand, can able to provide precise observation of the morphology, crystal structure, and distribution of the nanoparticles. TEM images of GO and its composite samples are shown in Fig. 3e–h. Micrograph of GO, in Fig. 3e, shows that the GO sheet are locally crumpled which could be attributed to different nucleation growth rate of particles. TiO_2 nanoparticles are thin and transparent with an average particle size distribution of 20–30 nm (Fig. 3f). On the other hand, Fig. 3 g and h) indicate that the TiO_2 nanoparticles are attached onto the rGO surface which form a composite structure.

4.3 Fourier transform infrared and Raman analysis

FTIR analysis is helpful in material characterization. Functionalized GO, prepared by modified Hummers' method, and reduction of GO to rGO in hydrothermal treatment form composite structure bridged with TiO_2. Figure 4 shows the FTIR spectra of GO and rGO–TiO_2 composites. The FTIR spectra of GO shows various peaks that can be attributed to the presence of oxygen-containing functional groups in the material. The bands at 1034 cm^{-1} shows the stretching vibration, $\nu(C–O)_{str}$, of alkoxy functional groups. The peaks at 1192 and 1405 cm^{-1} indicated the presence of $\nu(C–O–C)_{str}$ and $\nu(C–O)_{str}$ vibration of carboxyl groups, respectively. A peak at 1270 cm^{-1} is attributed to the $\nu(C–O)_{str}$ vibrational frequency of epoxy functional group. The absorption peak at 1720 cm^{-1} corresponds to $\nu(C=O)_{str}$ vibration of carboxyl functional groups. A broad peak observed at 3400 cm^{-1} and the presence of peak at 1630 cm^{-1} corresponds to the stretching vibrational and bending vibrational frequencies, respectively, of hydroxyl functional groups of H_2O molecules which could got adsorbed/attached to surface of graphene

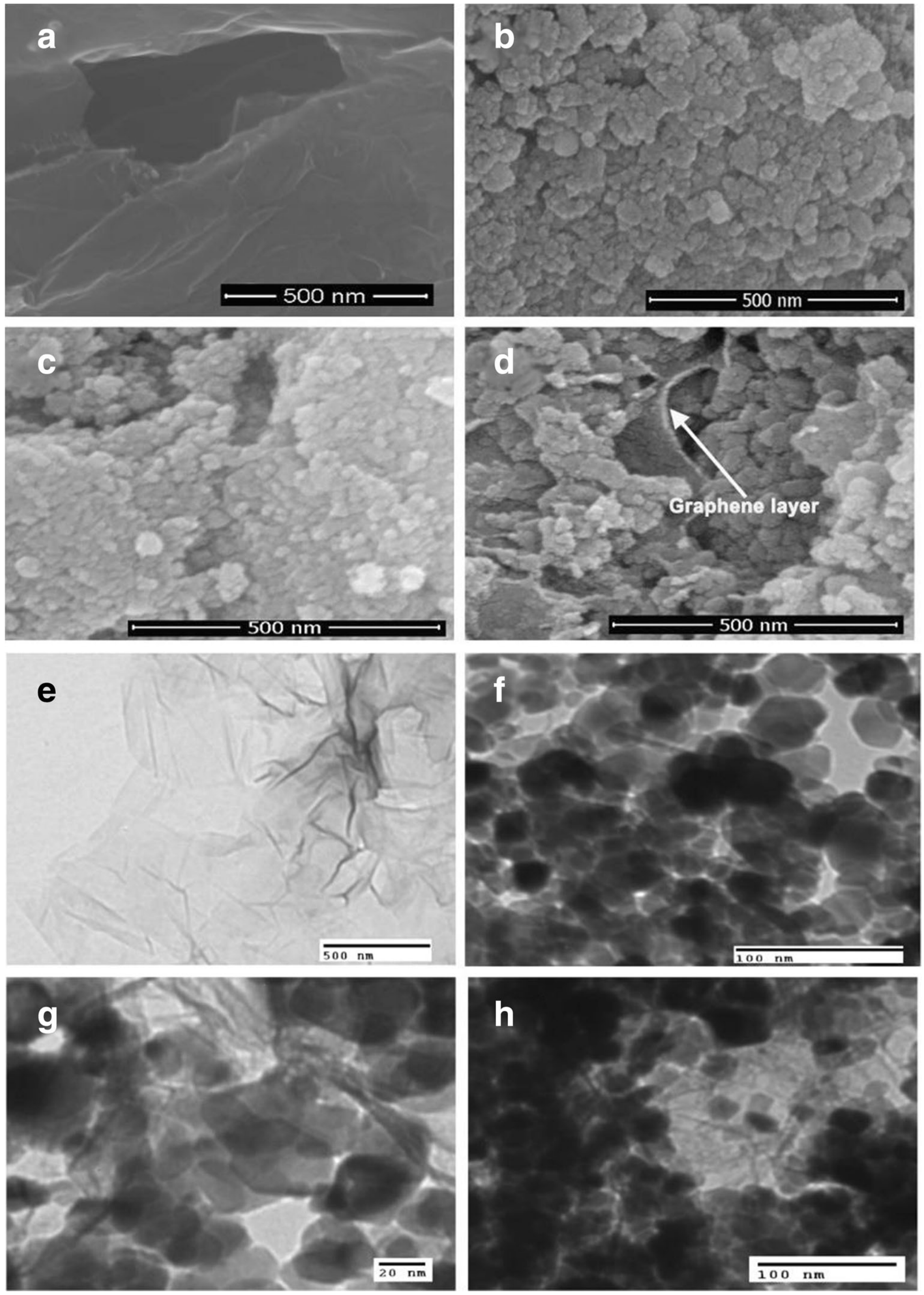

Fig. 3 SEM images. **a** GO. **b** pristine TiO_2. **c** rGO(1 wt%)–TiO_2. **d** rGO(4 wt%)–TiO_2. TEM images. **e** GO. **f** Pristine TiO_2. **g** rGO(1 wt%)–TiO_2. **h** rGO(4 wt%)–TiO_2

oxide. The presence of absorption peaks at 2900 cm^{-1} and 2687 cm^{-1}, respectively, are related to both symmetric and anti-symmetric stretching vibrations of methylene (–CH_2–) groups [33]. It may be noted that the peaks related to the presence of functional groups containing oxygen is absent, in case of nanocomposites, indicating reduction of GO to rGO. Further, rGO–TiO_2 nanocomposites shows additional peaks within 400–500 cm^{-1}, which attributed to the presence of TiO_2 in the moiety [34]. It is presumed that the functional groups available in GO act as active sites for interfacial interaction with TiO_2 in order to form stable composites structure.

Raman analysis is carried out to understand more about functionalization of graphite, particularly the formation of GO. The Raman spectra of sample materials is shown in Fig. 5. GO sample shows the typical D band at 1340 cm^{-1} attributed to the defects and in-plane vibration of sp^2 bonded carbon atom in GO network structure; whereas, peak at 1610 cm^{-1}, referred to G band, is primarily due to formation

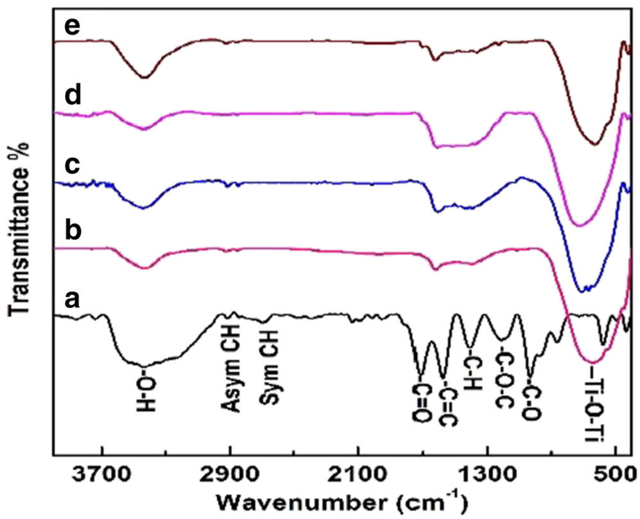

Fig. 4 FTIR spectra of (a) GO, (b) TiO_2, and TiO_2 with GO (c) 0.5, (d) 1.0, and (e) 4.0 wt% substitution

of ordered graphitic structure [28, 35]. The spectrum of pristine TiO_2 is also furnished in Fig. 5. It is reported that Raman bands observed at 143, 144, 235, 395, 445, 515, 612, and 638 cm^{-1} are attributed to typical vibration bands of TiO_2. Peaks at 143, 395, 515, and 639 cm^{-1} are ascribed to the presence of anatase–TiO_2 phase that corresponds to $E_{g(1)}$, $B_{1g(1)}$, $A_{1g} + B_{1g(2)}$, and $E_{g(2)}$ mode of vibrations [36]. Similarly, peaks observed at 144, 235, 446, and 613 cm^{-1} are attributed to B_{1g}, two-phonon scattering, E_g, and A_{1g} modes of vibration in rutile–TiO_2 phase, respectively. The D band and G band of graphene in rGO–TiO_2 composites were found to be shifted from their emblematic positions. Such kind shifts following change in the characteristic D/G intensity ratios could be attributed to surface strain which could happen due to the incorporation/immobilization of TiO_2 in rGO structure [37, 38], and the ratio of D/G is reported as inversely proportional to the average size of the sp^2 domains [27]. In

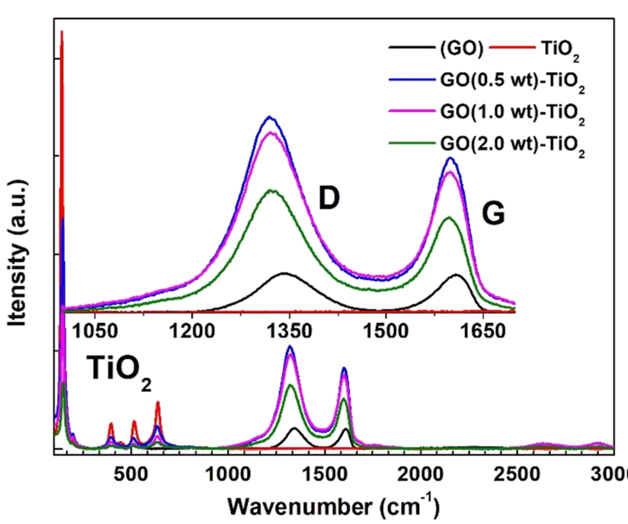

Fig. 5 Raman spectra of GO, TiO_2, and rGO–TiO_2 nanocomposites

this context, the rise in the D/G intensity ratios from 1.08 (in case of 0.5 wt% GO) to 1.24 (in case of 1% rGO) and 1.27 (in case of 2 wt% GO) indicates that the TiO_2 is successfully incorporated in GO sheets to form rGO–TiO_2 composite material. The addition of GO reduces the intensity of TiO_2 which is evident from Raman active modes of vibration that indicates changes through substitution of one or more Π-bonds of GO.

4.4 X-ray photoelectron analysis

X-ray photoelectron spectroscopy (XPS) can provide valuable information related to the surface chemical structure of the material. The XPS spectra of rGO–TiO_2 nanocomposites are furnished in Fig. 6. The full survey spectrum of 1 wt% GO with TiO2 (Fig. 6a) shows strong Ti (Ti_{2p}), O (O_{1s}), and C (C_{1s}) peaks. Similarly, XPS spectra in Fig. 6 b and c show high resolution presence of C and O in GO sample material. The Ti spectrum is furnished in Fig. 6c, and the presence of the C, O, and Ti in survey spectra supports the formation of rGO–TiO_2. However, the peak intensity of oxygenated carbon was found to be more than the C–C as shown in Fig. 6b, indicating the conversion of graphite into graphene oxide [39]. The peak position of the C–C, C=O, and C–OH species in GO are observed with binding energy of 284.1, 286.7, and 287.6 eV, respectively. Similar peaks are also observed in rGO–TiO_2 which could be attributed to the presence of residual oxygenated groups. High-resolution Ti (2p) spectrum corresponds to the presence of Ti^{4+}, indicating that the TiO_2 remains intact in characteristic crystal structure during the process. The bands located at energies of 457.9 eV (Ti $2p^{3/2}$) and 463.8 eV (Ti $2p^{1/2}$) were assigned to the O–Ti bond in TiO_2. The binding energy of the composite material, in summarized form, is presented in Table 1.

4.5 Charge carrier transportation study

Figure 7 shows the diffuse reflectance UV–Vis optical response spectra of GO and rGO–TiO_2 studied in the range of 200–600 nm. The pristine TiO_2 sample, in Fig. 7a, shows an absorption edge at around 320 nm (UV range) attributed to electronic transitions from O_{2p} to Ti_{3d} level in TiO_2 [40]. Titanium shows significant UV region absorption, and the band gap was calculated to be 3.12 eV. The addition of small amount of rGO in TiO_2 shows a red shift in absorption edge with significant improvement in the absorption intensity in UV region with broad absorption in visible region. The maximum absorption was recorded in case of TiO_2 incorporated with 1 wt% GO. Improvement in absorption intensity supports the fact of more accumulation of the electron density at material surface facilitating effective electron transfer. Existence of heterostructure at the material surface also manifest visibly from change in color of the material (Fig. 1) and shifting in the peak positions in the spectra. Incorporation of rGO also

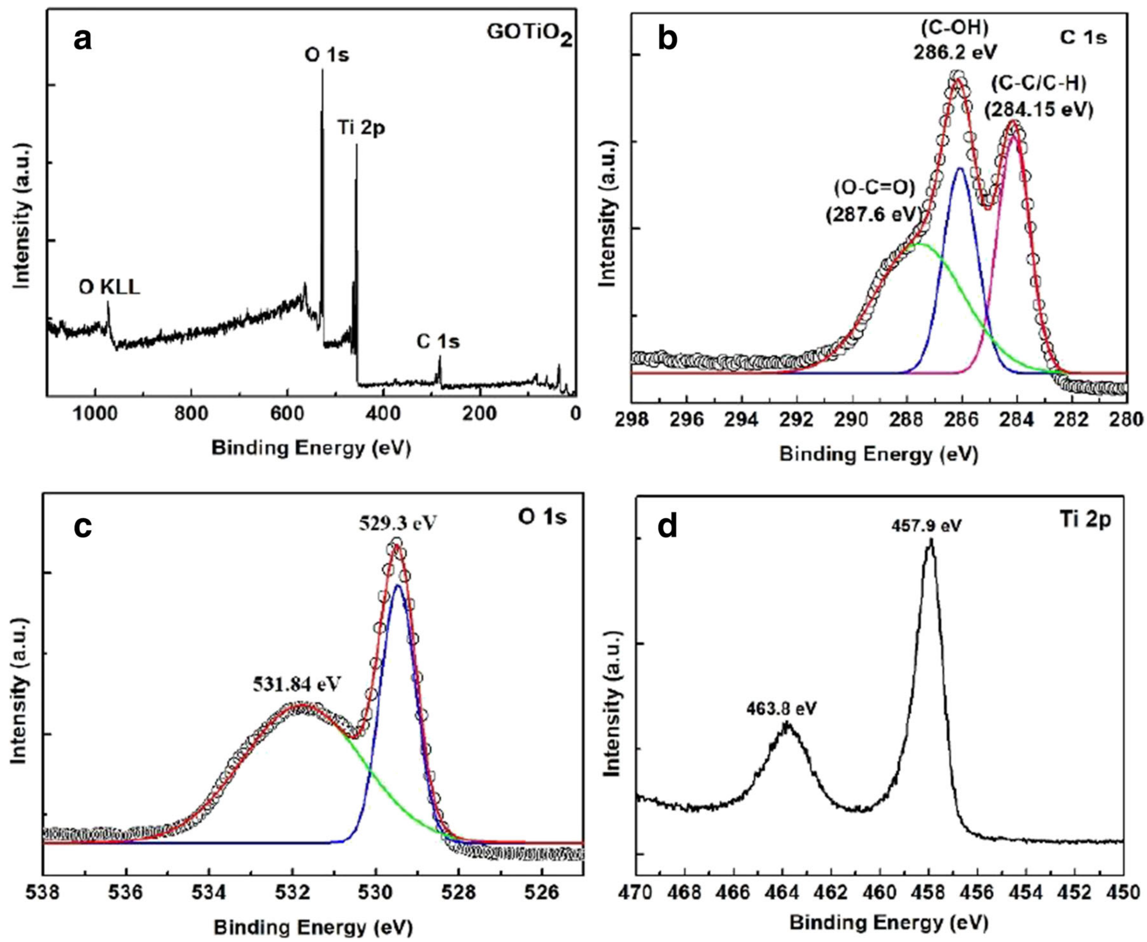

Fig. 6 XPS (**a**) survey spectra and close spectra of (**b**) C(1s), (**c**) O(1s), and (**d**) Ti (2p) peaks

modify the band gap energy of TiO_2, where the estimated band gap energy is reduced from 3.12 eV (TiO_2) to 2.89 eV (0.5 wt% rGO–TiO_2). The band gap further changes to 2.99 eV or 2 wt% rGO–TiO_2. The narrowing of band gap in case of rGO–TiO_2 nanocomposites (with different wt% of rGO) could be related to Ti–C covalent bond formation for the case of rGO–TiO_2 sample.

The photoluminescence (PL) emission spectra of the sample materials is furnished in Fig. 8. The spectra were recorded at excitation wavelength of 275 nm. The PL spectra could correlate the photo-generated electron-hole separation and recombination efficiency, which is essential for study of photocatalytic properties of the material. The high intensity emission peak in TiO_2 nanoparticles is observed at 403 nm, which could be originated from free excitation of electron, i.e., direct electrons transition from valence to conduction band. Few other peaks, with variation in intensities, are observed at 421, 442, 483, 536 nm that could be attributed to Schottky barrier formation at metal nanoparticles and substrate interface [41]. Increase in amount of GO in composite materials gradually reduces the peak emission intensities. Therefore, increasing the GO contents in rGO–TiO_2 nanocomposites and

Table 1 Binding energy vs chemical bond species for GO and rGO-TiO_2/binary heterostructure

Elements	GO (eV)	Chemical bond species	rGOTiO$_2$ (eV)	Chemical bond species
Ti $2P_{3/2}$	-	-	457.9	Ti–O
Ti $2P_{1/2}$	-	-	463.8	Ti–O
O 1s A	529.3	C–O	529.3	Lattice oxygen (Ti–O)
O 1s B	531.8	C=O	531.8	Surface hydroxyl (Ti–OH)
C 1s A	284.8	C–C/C–H	283.9	C–C/C–H
C 1s B	286.2	C–OH/C–O–C	285.4	C–OH/C–O–C
C 1s A	287.6	O–C=O	286.5	O–C=O

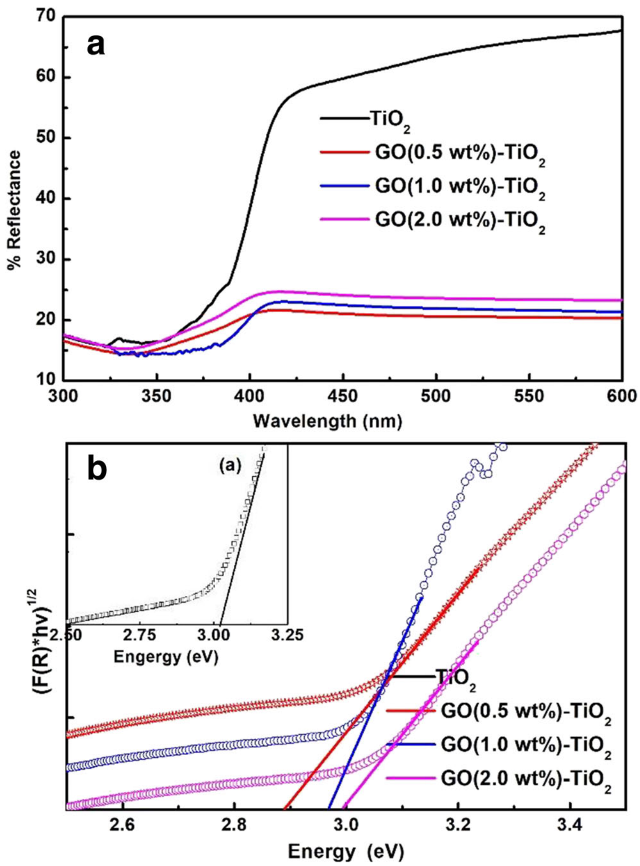

Fig.7 **a** Diffuse reflectance spectra and **b** band gap of rGO–TiO_2 nanocomposites

corresponding reduction in emission intensity indicates that the presence of GO effectively lowering the rate of recombination of photo-induced charge carriers (electron-hole pairs) by formation of Schottky barrier at the rGO–TiO_2 interface. Further, it is evident that during the electronic transition process, the composite material could behave either as an electron sinker or transporter efficiently. It is to be noted that such electronic transition mostly depend on charge carriers density and their transition probability from excited energy state to ground energy state. It also signifies that the rGO–TiO_2 possess longer carriers lifetime due to the rapid charge transport in rGO network. The enhancement in charge carrier lifetime is possibly due to transfer of excited electrons from conduction band of TiO_2 to rGO sheets averting the possible direct electron-hole recombination. Inhibition of electron-hole recombination behavior is essential for materials to exhibit properties for the photocatalytic applications. Therefore, the result indicates that chemically bonding interface of rGO and TiO_2 composite enabled the charge separation and transportation during photo-irradiation process.

Further, electrochemical impedance spectroscopy (EIS) measurement was conducted to show the interfacial charge transfer process in TiO_2 and rGO–TiO_2 composite material. Figure 9 presents the Nyquist plots of TiO_2 and rGO–TiO_2 nanocomposites to illustrate the influence of rGO on separation and migration of electron-hole pairs. In Fig. 9, the diameter of the Nyquist semicircle reveals the charge transport and recombination properties of the material. In present investigation, the semicircle of TiO_2 was found to be larger than that of the rGO–TiO_2. The charge transfer resistance (R_{CT}) estimated from the semicircle diameters shows that the rGO–TiO_2 composite (~4 Ω) has a lower R_{CT} value than TiO_2 (~26 Ω). It indicates the rGO–TiO_2 composite increases the charge transportation and reduces the recombination rate which is in good agreement with reported photoluminescence values [42, 43]. Hence, it is evident that the enhanced charge transfer process in case of rGO–TiO_2 could improve the separation efficiency of charge carriers (electron-hole pairs) resulting in longer carrier lifetimes, thereby improving in photocatalytic activity of the material.

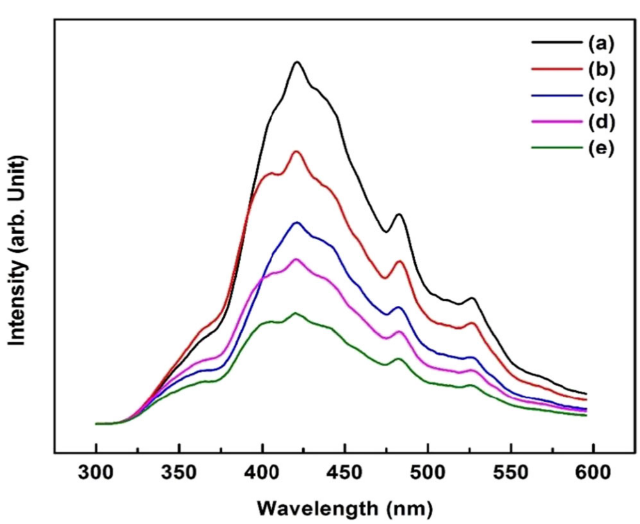

Fig. 8 Photoluminescence spectra of pure and rGO–TiO_2 samples

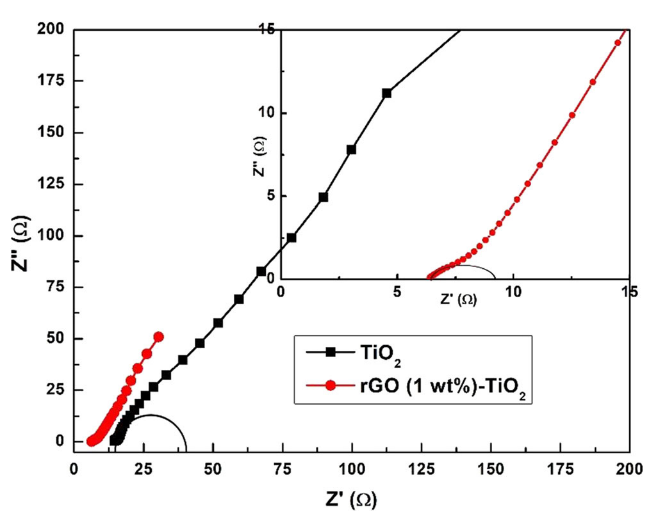

Fig. 9 Nyquist plots of pure TiO_2 and rGO–TiO_2 nanocomposite samples

4.6 Photocatalytic methylene blue degradation

The material was tested for its photocatalytic activities for degradation of organic dye. It is known that organic dye is one of the important component for coloring and printing applications in industries. The industrial effluent often contain organic dyes creating environmental concern. The degradation of dyes resulted in toxic byproducts causing severe water pollution affecting human being as well as various aquatic species. Photocatalytic degradation of selected MB dye was attempted using newly prepared composite material (rGO–TiO_2). The experiment was conducted in the presence of simulated solar light, i.e., in the presence of UV–Vis irradiation, as well as in the absence of light. Figure 10 shows degradation behaviors of MB dye in the presence of TiO_2 and rGO–TiO_2.

The degradation characteristics of MB dye in the presence of rGO–TiO_2 catalyst was studied spectrophotometrically from relative concentration/absorbance ($\lambda_{(max)} = 663$ nm) change of the dye solution using calibration curve. It is observed that rGO–TiO_2 could be able to degrade MB solution in the absence of light (Fig. 10c). However, TiO_2 nanoparticles shows no apparent change in spectra even within 60-min time period (Fig. 10b) under same experimental condition.

In this aspect, Fig. 10d shows that the characteristic absorption peak of MB dye decreases and finally disappeared after 60 min. Figure 10 a and b also show the qualitative aspects of degradation of MB molecules (85–97%) using rGO–TiO_2. Table 2 provides a comparative account of degradation efficiency of various materials under consideration. rGO–TiO_2 shows better photocatalytic activity than bare TiO_2. Methylene blue is a photoactive phenothiazine dye. In the presence of rGO–TiO_2 and light irradiation, it is possible that synergetic competitive processes such as demethylation of MB dye followed by decomposition of the aromatic rings in dye molecule could take place thus degrading the entire molecule [44].

The kinetics of photocatalytic degradation was studied using Eq. 2 [45, 46]:

$$\text{Rate} = -\frac{dc}{dt} = KC \tag{2}$$

where, K and C are the rate constant and concentration of the solution, respectively. The plot of (C_t/C_0) versus time (minutes), in Fig. 11 a and b, and corresponding logarithmic plots (Fig.11 c and d show the degradation rate of MB. The slope of the plot yielded a value of rate constant as 0.07622 min^{-1} for rGO(1 wt%)–TiO_2 which corroborated to the kinetics of 1st order reaction. Among all the prepared catalysts, rGO–TiO_2 (with 1.0 wt% of GO) shows excellent photocatalytic activity, where almost 97% MB degradation was observed in 60 min time interval (Fig. 11b). Table 2 shows the degradation values of MB dye in the presence of photocatalytic materials. rGO–

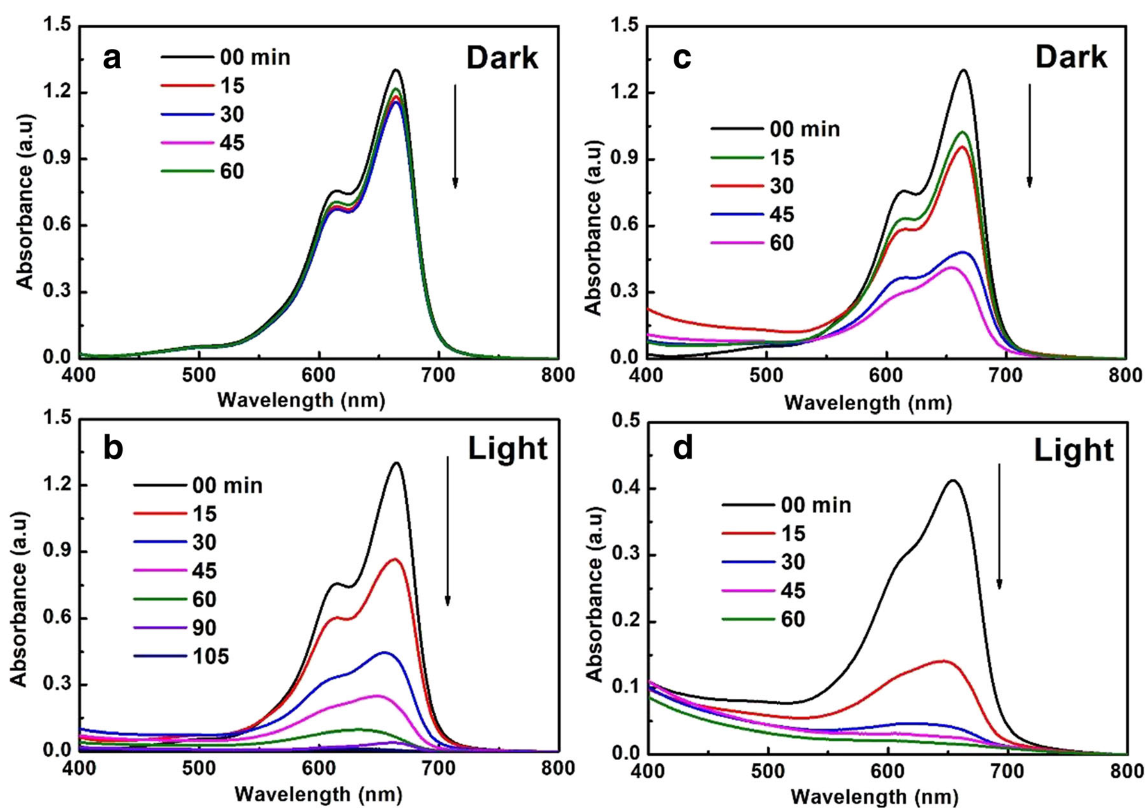

Fig. 10 UV–visible absorption spectra of methylene blue (**a**, **b**) for TIO_2 and (**c**, **d**) for rGO(1 wt%)–TiO_2

Table 2 Optical response and photocatalytic activity of TiO_2 and its composite with rGO

S. no.	Photo-catalysts	Band gap (eV)	Degradation rate constant (min^{-1})		Hydrogen production (μmol)
			Dark	UV-visible irradiation	
1	Pure TiO_2	3.12	0.00178	0.03422	173
2	rGO(0.5 wt%)–TiO_2	2.89	0.01644	0.07422	190
3	rGO(1.0 wt%)–TiO_2	2.97	0.01800	0.07622	838
4	rGO(2.0 wt%)–TiO_2	2.99	0.01511	0.06222	106
5	rGO(4.0 wt%)–TiO_2	3.02	0.01089	0.04733	339

TiO_2 nanocomposites show enhanced photocatalytic activity in the absence of light/irradiation. The decrease in concentration of MB in the absence of light could also be due to adsorption of MB upon the surface of photocatalytic material in addition to degradation process.

4.7 Photocatalytic hydrogen production

The prepared materials were used for production of hydrogen from photocatalytic splitting of water molecules. Both TiO_2 and rGO–TiO_2 sample materials were used for the production of hydrogen under equal conditions of illumination with simulated solar source. The experimental set up for photocatalytic hydrogen production is furnished as supporting information (S1). The results of the experiment regarding hydrogen evolution is furnished in Fig. 12.

It is interesting to note that in case of rGO–TiO_2, the quantity of hydrogen production is higher than that of pure TiO_2 sample material. Pure TiO_2 produces 173 μmol of H_2 and the rate of hydrogen production was 35 μmol/h. The low photocatalytic activity for pure TiO_2 could be attributed to quick recombination between core-bonded (CB) electrons and valence bond (VB) holes facilitated by generation of large over potential during H_2 generation. GO(1 wt%)–TiO_2, on the other hand, promotes available photo-excited electrons for proton reduction, and the result is in consistent with the UV–Vis spectra (Fig. 7a) indicating high absorption intensity resulting in high H_2 production rate. As the GO loading is increased from 0.5 to 1 wt%, the H_2 production is also increased from

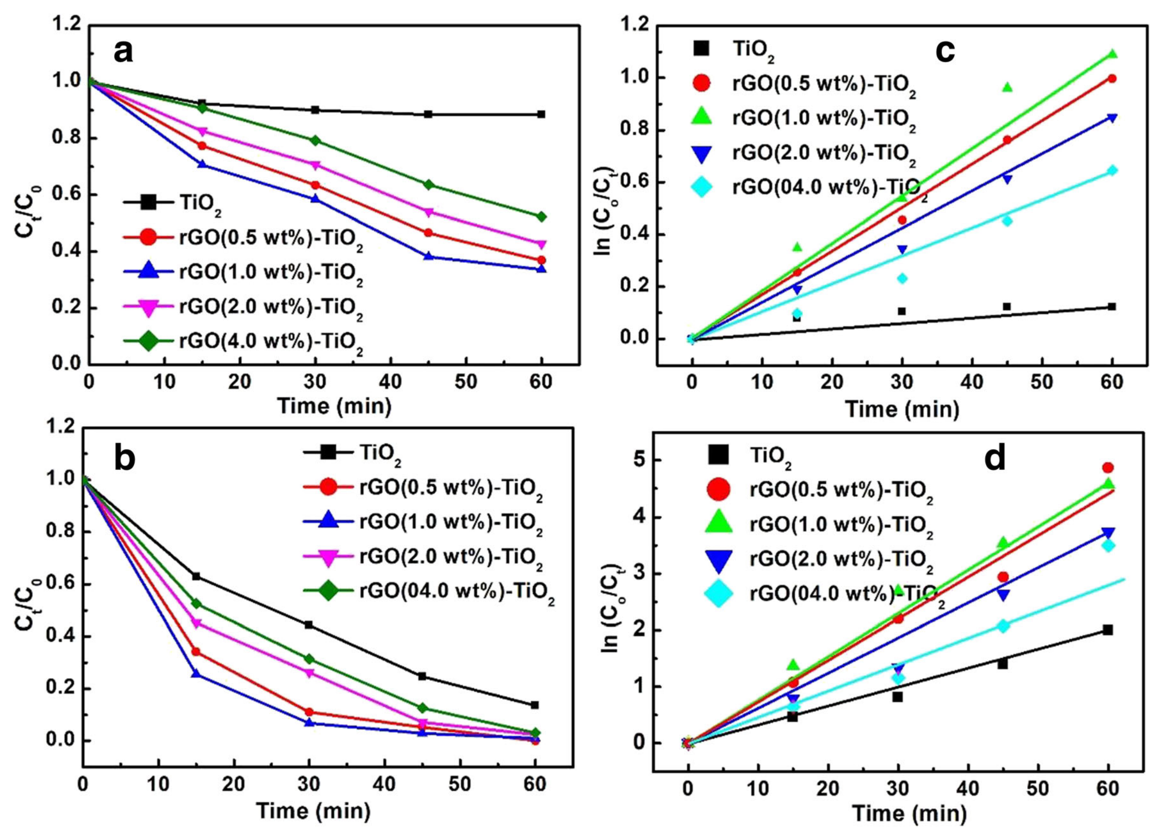

Fig. 11 Study of degradation efficiency with respect to irradiation time. **a** and **c** In the absence of light. **b** and **d** In the presence of light

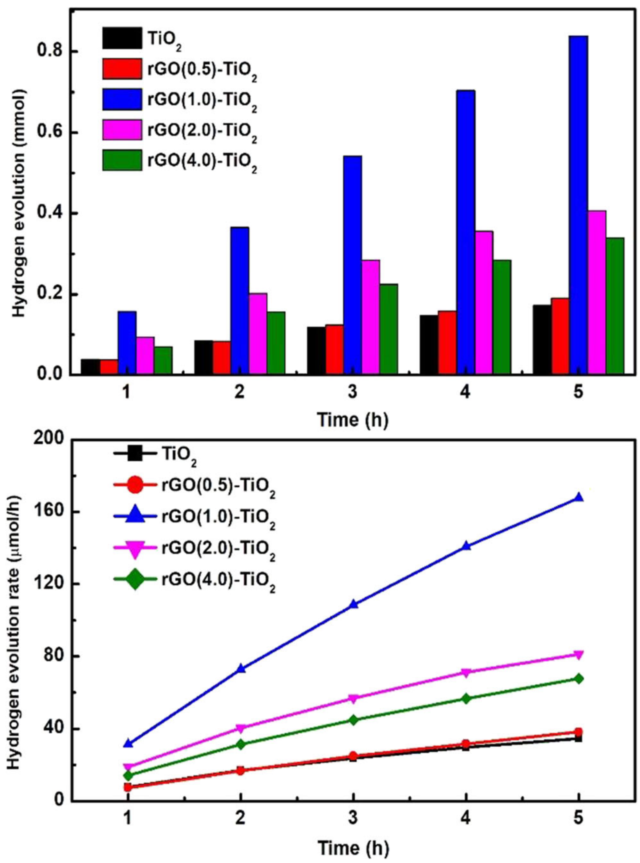

Fig. 12 Photocatalytic water splitting in presence of photocatalysts

190 to 838 mmol which is five times higher than pristine TiO_2. TiO_2–GO (1.0 wt%) shows highest 168 μmol/h H_2 production. With increment in GO loading, i.e., TiO_2–GO (2%), the amount of H_2 production was found to decrease. Increase in amount of graphene in the composite material reduces the photocatalytic activity of the material. In this context, graphene content of 4.0 wt% in the composite material could significantly reduce the photocatalytic properties of the material. The reason could be attributed to the statistic that higher amount of graphene block the surface active sites of TiO_2 photocatalyst, therefore, shields the sites from receiving incident photons; subsequently, a rapid decrease in H_2 production is observed (Fig. 12). The study indicates that an optimized loading of graphene to TiO_2 is crucial for optimizing the photocatalytic behavior of graphene–TiO_2 composites for efficient hydrogen production and pollutant degradation. In this aspect, Table 2 shows the hydrogen production rate of different sample materials.

4.8 Mechanism of charge separation and transportation process in photocatalyst for hydrogen evolution and pollutant degradation

Charge separation and transportation in semiconductor photocatalyst depends on the subjugation of the recombination center of the excited charge carriers in response to incident solar light radiation. Normally, traditional semiconductors exhibit poor response to light radiation due to fast recombination of charge carriers. Response to light can be improved by developing a photocatalyst which has heterostructure surface with a suitable potential energy barrier. In the present study, GO was used to build Schottky barrier that facilitate the electron restoration by providing chemically active sites, where chemical changes can ensue due to low activation energy barrier. Therefore, use of GO serve as a support and/or anchored material for the immobilization of TiO_2 particles in addition to its activity towards inhibiting further accretion of TiO_2 upon material surface.

Figure 8 shows the photoluminescence emission spectra of the composites. The PL intensity is related to the amount of charge carriers (electron-hole pairs) recombination process. At constant or common excitation irradiation, PL peak at 403 nm which aroused from the recombination of photo-generated electron-hole pairs. It may be noted that PL intensity of the same peak in rGO–TiO_2 noticeably decreases after bridging TiO_2 on the rGO surface, which could be attributed to the transfer of electron from the TiO_2 surface to the rGO surface on account of their closely acquainted interfacial contact and favorable energy level configuration. Further, the lesser emission intensity indicate that electron-hole pairs are trapped or recombined via a radiation-less path or process, or transferred at the particle surface. The above process can be expressed in terms of photo-generated conduction band electrons in the following manner:

$\mathrm{Excited}_{\mathrm{electron}} = \mathrm{Trap}_{\mathrm{electron}} + N_{\mathrm{electron}} + R_{\mathrm{electron}} + \mathrm{Tran}_{\mathrm{electron}}$.

The above equation represents that the electrons which are primarily get excited after they trapped at defect sites (trap), recombined via a non-radiative (N) pathway, recombined (R) with PL (rad), or transferred at the interface. The maximum photo–catalytic activity results from the ratio of the transfer electron to the excited electron. Therefore, higher photocatalytic activity is related to poorer emission intensity, only if, the sum of the trapped electron and the non-radiative electron remains relatively constant. But, the higher graphene contents TiO_2 materials could be an exclusion to the above assumption even though having poorer emission intensity. This implies that the trapped electron and the non-radiative electron is higher in other materials than the rGO(1 wt%)–TiO_2 because it could show the presence of a larger number of defect sites that enhances the trapped electron and the non-radiative electron as confirmed by increasing the defect (D) band in Raman spectra. This is also observed in UV–Vis spectra in terms of enhancement in absorption intensity (Fig. 7a). The process resulted in delaying the recombination of the reactive electrons and holes lifetime, thus increasing the photocatalytic activity of the material. The suppression of charge recombination and enhancement of electron acceptance and transportation is further confirmed by study of EIS of the material through reduction in the charge transfer resistance in rGO–TiO_2 interface layer (Fig. 9). The proposed mechanism of photocatalysis for H_2 generation and MB degradation using rGO–TiO_2 composite is presented in Scheme 2.

In this context, it is understood that the hybridization of rGO–TiO_2 effectively lower the overall band gap (Fig. 7b) in order to improve the light absorption capacity, which in turn facilitate the creation of a large number of electron-hole pairs. Using the band gap measurement, the E_{VB} (valence band edge potential) and E_{CB} (conduction band edge potential) potential of TiO_2 nanoparticles and rGO were calculated using the following equations [46]:

$$E_{VB} = X - E_0 + \frac{1}{2} E_g \quad (3)$$

$$E_{CB} = E_{VB} - E_g \quad (4)$$

where electronegativity (X) values of the TiO_2 semiconductor is 5.81 eV [46, 47]. The free electrons energy (E_O) on the hydrogen scale is 4.5 eV. The band gap (E_g) of TiO_2 was measured to be 3.12 eV. The E_{CB} and E_{VB} edges of TiO_2 and rGO were estimated by using these values in the above equations and the corresponding energy band diagram of rGO–TiO_2 heterostructure is shown in Scheme 2b. The study suggests that the E_{CB} and E_{VB} edges of TiO_2 are more negative and positive than rGO. Therefore, electrons inject from the CB of TiO_2 to rGO resulted in the separation of electrons and holes, because graphene can act as a trapper for the photogenerated electron due to the much lower Fermi energy of graphene than the E_{CB} of TiO_2. Therefore, the excited electrons can be stored in the graphene nanosheets π–π network in the composites that helps in retarding the electron-hole pairs recombination on TiO_2 surface. This process could facilitate effective interface charge separation and, therefore, deters charge carrier recombination process. The electron transfer process between TiO_2 and graphene nanosheets can be expressed as

$$TiO_2 + h\nu \rightarrow e^-(CB, TiO_2) + h^+(VB, TiO_2)$$

$$Graphene + e^-(CB, TiO_2) \rightarrow e^-(Graphene) + TiO_2$$

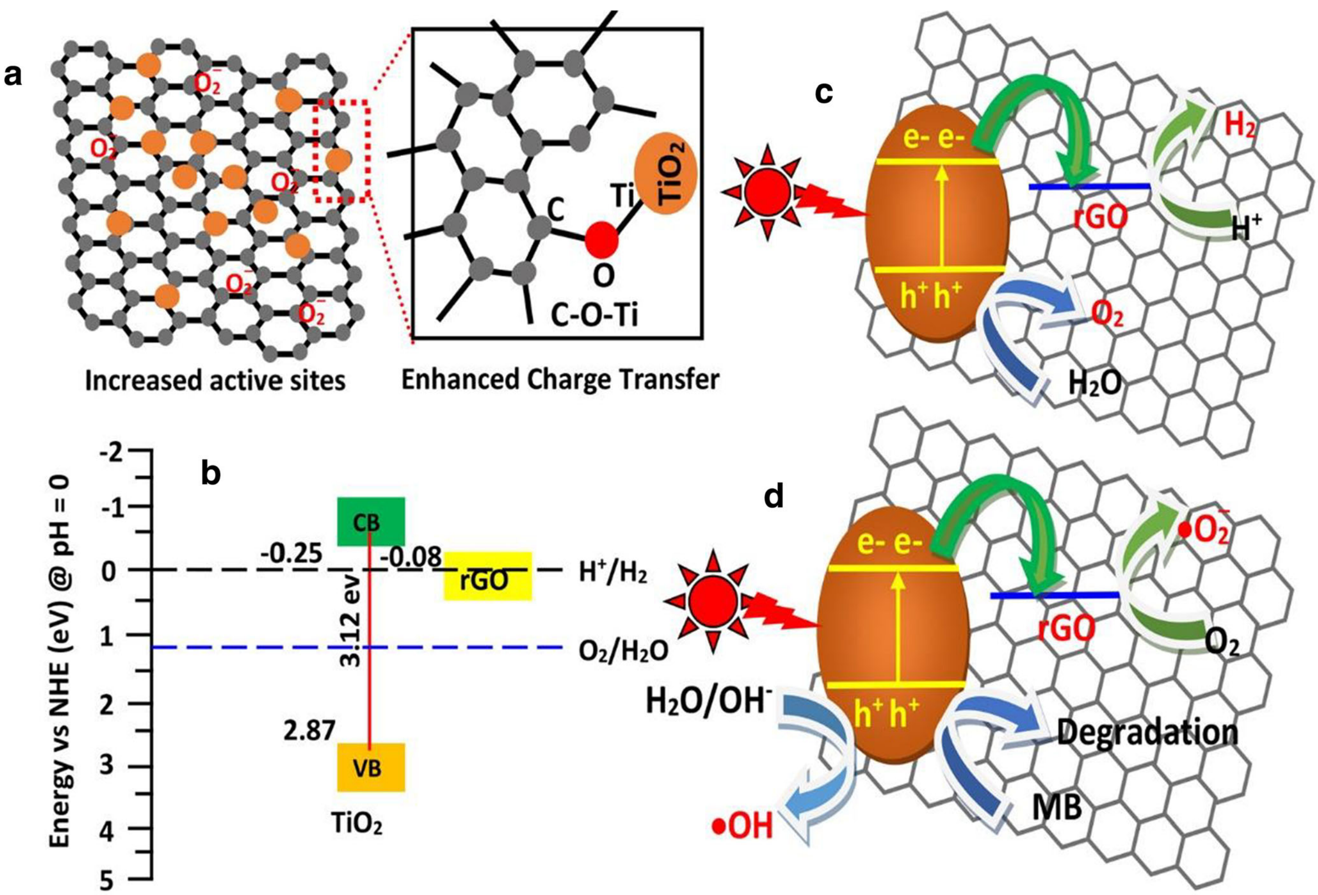

Scheme 2 Schematic illustrations of (**a**) the formation of Ti–O–C bond in the separation-free rGO–TiO_2 catalyst and the photocatalytic process, (**b**) energy band diagram of TiO_2 and rGO, charge transfer for (**c**) photocatalytic H_2 production on rGO-TiO_2, and (**d**) photocatalytic methylene blue dye degradation

It may be noted that electrons can efficiently reduce protons to molecular hydrogen (H_2) at the surface of rGO, and photogenerated holes get scavenged by methanol solution at the TiO_2 surface which is demonstrated in Scheme 2c.

Furthermore, the pathway of the decomposition of the dye in the presence of photocatalyst is presented in Scheme 2d. It shows that the degradation proceeds through three different modes, i.e., excitation/sensitization followed by transportation and degradation process. The self-sensitization of MB molecule upon the surface of catalyst happens due to transfer of electrons from TiO_2 to rGO. The transported electrons further interacts with the dissolved oxygen to generate the reactive oxygen radical anion ($\bullet O_2^-$), and the highly unstable reactive species in aqueous solution can be converted to hydroxyl radical ($OH^\bullet$) species. The hydroxyl radical facilitates degradation of MB dye under illumination/radiation.

5 Conclusions

In the present study, a series of rGO–TiO_2 heterostructured nanocomposites were synthesized and studied for their enhanced photocatalytic activities for the production of H_2 as well as for the degradation of methylene blue dye. The enhanced photocatalytic activities of the materials were attributed to the promotion of charge separation. Quenching of the emission spectra in the presence of rGO indicate the ability of rGO to delay the recombination of photo-excited charge carriers. Composite material with TiO_2 and GO content (from 0.5 to 1 wt%) facilitate enhanced H_2 production, i.e., from 190 to 838 mmol. Enhanced GO loading, however, shows reduction in the production of H_2 which could be attributed to shielding of active sites of TiO_2. rGO(1 wt%)–TiO_2 effectively maximize hydrogen production rate to 168 μmol/h and MB degradation to 0.07622/min. The study indicates that TiO_2–rGO could efficiently inhibit the recombination center of electron-hole pairs of semiconductors.

Acknowledgments The authors express their gratitude to the Central Instrumentation Facilities (CIF) of Birla Institute of Technology, Mesra, Ranchi.

Compliance with ethical standard

Conflict of interest The authors declare that they have no competing interest.

References

1. Fujishima A, Honda K (1972) Electrochemical photolysis of water at a semiconductor electrode. Nature 238:37–38
2. Grätzel M (1983) Energy resources through photochemistry and catalysis, 1st edn. Academic Press, New York
3. Zhang A-Y, Wang W-Y, Chen J-J, Liu C, Li Q-X, Zhang X, Li W-W, Si Y, Yu H-Q (2018) Epitaxial facet junctions on TiO_2 single crystals for efficient photocatalytic water splitting. Energy Environ Sci 11:1444–1448
4. Zhang Z, Xu B, Wang X (2014) Engineering nanointerfaces for nanocatalysis. Chem Soc Rev 43:7870–7886
5. George S, Pokhrel S, Ji Z, Henderson BL, Xia T, Li L, Zink JI, Nel AE, Mädler L (2011) Role of Fe doping in tuning the band gap of TiO_2 for the photo-oxidation-induced cytotoxicity paradigm. J Am Chem Soc 133:11270–11278
6. Yang Y, Wen J, Wei J, Xiong R, Shi J, Pan C (2013) Polypyrrole-decorated Ag-TiO_2 nanofibers exhibiting enhanced photocatalytic activity under visible-light illumination. ACS Appl Mater Interfaces 5:6201–6207
7. Sahoo R, Roy A, Ray C, Mondal C, Negishi Y, Yusuf SM, Pal A, Pal T (2014) Decoration of Fe_3O_4 base material with Pd loaded CdS nanoparticle for superior photocatalytic efficiency. J Phys Chem C 118:11485–11494
8. Chen Z, Xu Y-J (2013) Ultrathin TiO_2 layer-coated CdS spheres core-shell nanocomposite with enhanced visible-light photoactivity. ACS Appl Mater Interfaces 5:13353–13363
9. Ranjeesh KC, George L, Wakchaure VC, Goudappagouda G, Devi RN, Santhosh Babu S (2019) A squaraine-linked metalloporphyrin two-dimensional polymer photocatalyst for hydrogen and oxygen evolution reactions. Chem Commun 55:1627–1630
10. Wang Z, Li C, Domen K (2019) Recent developments in heterogeneous photocatalysts for solar-driven overall water splitting. Chem Soc Rev 48:2109–2125
11. Lin Y, Li D, Hu J, Xiao G, Wang J, Li W, Fu X (2012) Highly efficient photocatalytic degradation of organic pollutants by PANI-modified TiO_2 composite. J Phys Chem C 116:5764–5752
12. Wu H, Tseng PY, Hsieh PY, Chou HT, Tai NH (2015) High mobility of graphene-based flexible transparent field effect transistors doped with TiO_2 and nitrogen-doped TiO_2. ACS Appl Mater Interfaces 7:9453–9461
13. Mao J, Ge M, Huang J, Lai Y, Lin C, Zhang K, Meng K, Tang Y (2017) Constructing multifunctional MOF@rGO hydro-/aerogels by the self-assembly process for customized water remediation. J Mater Chem A 5:11873–11881
14. Li H, Wu Y, Li C, Gong Y, Niu L, Liu X, Jiang Q, Sun C, Xu S (2019) Design of Pt/t-ZrO_2/g-C_3N_4 efficient photocatalyst for the hydrogen evolution reaction. Appl Catal B Environ 251:305–312
15. Bera R, Kundu S, Patra A (2015) 2D hybrid nanostructure of reduced graphene oxide–CdS nanosheet for enhanced photocatalysis. ACS Appl Mater Interfaces 7:13251–13259
16. Akhavan O (2010) Graphene nanomesh by ZnO nanorod photocatalysts. ACS Nano 4:4174–4180
17. Pu YC, Wang G, Chang KD, Ling Y, Lin YK, Fitzmorris BC, Liu CM, Lu X, Tong Y, Zhang JZ, Hsu YJ, Li Y (2013) Au nanostructure-decorated TiO_2 nanowires exhibiting photoactivity across entire UV-visible region for photoelectrochemical water splitting. Nano Lett 13:3817–3823
18. Inturi SNR, Suidan M, Smirniotis PG (2016) Influence of synthesis method on leaching of the Cr-TiO_2 catalyst for visible light liquid phase photocatalysis and their stability. Appl Catalysis B: Environ 180:351–361
19. Hao R, Wang G, Tang H, Sun L, Xu C, Han D (2016) Template-free preparation of macro/mesoporous g-C_3N_4/TiO_2 heterojunction photocatalysts with enhanced visible light photocatalytic activity. Appl Catal B Environ 187:47–58
20. Tang Y, Jiang Z, Tay Q, Deng J, Lai Y, Gong D, Dong Z, Chen Z (2012) Visible-light plasmonic photocatalyst anchored on titanate nanotubes: a novel nanohybrid with synergistic effects of adsorption and degradation. RSC Adv 2:9406–9414

21. Wang J, Tafen DN, Lewis JP, Hong Z, Manivannan A, Zhi M, Li M, Wu N (2009) Origin of photocatalytic activity of nitrogen-doped TiO_2 nanobelts. J Am Chem Soc 131:12290–12297
22. Dunnill CW, Parkin IP (2011) Nitrogen-doped TiO_2 thin films: photocatalytic applications for healthcare environments. Dalton Trans 40:1635–1640
23. Chen XB, Shen SH, Guo LJ, Mao SS (2010) Semiconductor-based photocatalytic hydrogen generation. Chem Rev 110:6503–6570
24. Liu XJ, Zeng P, Peng TY, Zhang CH, Deng KJ (2012) Preparation of multi-walled carbon nanotubes/$Cd_{0.8}Zn_{0.2}S$ nanocomposite and its photocatalytic hydrogen production under visible-light. Int J Hydrog Energy 37:1375–1384
25. Kudo A, Miseki Y (2009) Heterogeneous photocatalyst materials for water splitting. Chem Soc Rev 38:253–278
26. Schneider J, Bahnemann DW (2013) Undesired role of sacrificial reagents in photocatalysis. J Phys Chem Lett 4:3479–3483
27. Fang J, Xu L, Zhang Z, Yuan Y, Cao S, Wang Z, Yin L, Liao Y, Xue C (2013) Au@TiO_2-CdS ternary nanostructures for efficient visible-light-driven hydrogen generation. ACS Appl Mater Interfaces 5:8088–8092
28. William S, Jr H, Richard E, Offeman J (1958) Preparation of graphitic oxide. J Am Chem Soc 80:1339
29. Park S, An J, Potts JR, Velamakanni A, Murali S, Ruoff RS (2011) Hydrazine-reduction of graphite and graphene oxide. Carbon 49: 3019–3023
30. Thompson P, Cox DE, Hastings JB (1987) Rietveld refinement of Debye–Scherrer synchrotron X-ray data from Al_2O_3. J Appl Crystallogr 20:79–83
31. Holzwarth U, Gibson N (2011) The Scherrer equation versus the 'Debye-Scherrer equation. Nat Nanotechnol 6:534–534
32. Aleksandrzak M, Adamski P, Kukułka W, Zielinska B, Mijowska E (2015) Effect of graphene thickness on photocatalytic activity of TiO_2 – graphene nanocomposites. Applied Surface Sci 331:193–199
33. Ossonona BD, Bélange D (2017) Synthesis and characterization of sulfophenyl-functionalized reduced graphene oxide sheets. RSC Adv 7:27224–27234
34. Liu G, Yan X, Chen Z, Wang X, Wang L, Lu G-Q, Cheng H-M (2009) Synthesis of rutile–anatase core–shell structured TiO_2 for photocatalysis. J Mater Chem 19:6590–6596
35. King AAK, Davies BR, Noorbehesht N, Newman P, Church TL, Harris AT, Razal JM, Minett AI (2016) A new RAMAN metric for the characterisation of graphene oxide and its derivatives. Sci Rep 6:19491–19496
36. Yu JG, Ma TT, Liu SW (2011) Enhanced photocatalytic activity of mesoporous TiO_2 aggregates by embedding carbon nanotubes as electron-transfer channel. Phys Chem Chem Phys 13:3491–3501
37. Dutta S, Ray C, Sarkar S, Pradhan M, Negishi Y, Pal T (2013) Silver nanoparticle decorated reduced graphene oxide (rGo) nanosheet: a platform for SERS based low-level detection of uranyl ion. ACS Appl Mater Interfaces 5:8724–8732
38. Ma J, Wang X, Liu Y, Wu T, Liu Y, Guo Y, Li R, Sun X, Wu F, Li C, Gao J (2013) Reduction of graphene oxide with L-lysine to prepare reduced graphene oxide stabilized with polysaccharide polyelectrolyte. J Mater Chem A 1:2192–2201
39. Xu B, Yue S, Sui Z, Zhang X, Hou S, Cao G, Yang YG (2011) What is the choice for supercapacitors: graphene or graphene oxide? Energy Environ Sci 4:2826–2830
40. Wendt S, Sprunger PT, Lira E, Madsen GKH, Li Z, Hansen JØ, Matthiesen Blekinge-Rasmussen JA, Lægsgaard E, Hammer B, Besenbacher F (2008) The role of interstitial sites in the Ti3d defect state in the band gap of titania. Science 320:1755–1759
41. Cheng K, Han N, Su Y, Zhang J, Zhao J (2017) Schottky barrier at graphene/metal oxide interfaces: insight from first-principles calculations. Sci Rep 7:41771–41777
42. Liu L, Qi Y, Lu J, Lin S, An W, Liang Y, Cui W (2016) A stable Ag_3PO_4@g-C_3N_4 hybrid core@shell composite with enhanced visible light photocatalytic degradation. Appl Cata B: Environ 183: 133–141
43. Zhu Y, Wang Y, Ling Q, Zhu Y (2017) Enhancement of full-spectrum photocatalytic activity over $BiPO_4/Bi_2WO_6$ composites. Appl Catal B Environ 200:222–229
44. Rauf MA, Meetani MA, Khaleel A, Ahmed A (2010) Photocatalytic degradation of methylene blue using a mixed catalyst and product analysis by LC/MS. Chem Eng J 157:373–378
45. Aarthi T, Madras G (2007) Photocatalytic degradation of rhodamine dyes with nano-TiO_2. Industrial & Engineering Chemistry Res 46:7–14
46. Chen Y, Huang W, He D, Situ Y, Huang H (2014) Construction of heterostructured g-C_3N_4/Ag/TiO_2 microspheres with enhanced photocatalysis performance under visible-light irradiation. ACS Appl Mater Interfaces 6:14405–14414
47. Chen X, Li L, Zhang W, Li Y, Song Q, Dong L (2016) Fabricate globular flower-like $CuS/CdIn_2S_4/ZnIn_2S_4$ with high visible light response via microwave-assisted one–step method and its multipathway photoelectron migration properties for hydrogen evolution and pollutant degradation. ACS Sustain Chem Eng 4:6680–6688